Stabilizing Layered BiOBr Photoelectrocatalyst by Van Der Waals Heterojunction Strategy

Stabilizing Layered BiOBr Photoelectrocatalyst by Van Der Waals Heterojunction Strategy

Mengjiao Wang*[a], Silvio Osella[b], Bruno Torre[a], Matteo Crisci[c], Fabian Schmitz[c], Roberto Altieri[c], Enzo Di Fabrizio[a], Heinz Amenitsch[d], Barbara Sartori[d], Zheming Liu[e], Teresa Gatti[a], Francesco Lamberti*[f,g,h]

[a] Dr. M. Wang, Dr. B. Torre, Prof. E. Di Fabrizio, Prof. T. Gatti
Dipartimento Scienza Applicata e Tecnologia (DISAT)
Politecnico di Torino
Corso Duca degli Abruzzi 24, 10129, Torino, Italy
E-mail: mengjiao.wang@polito.it

[b] Prof. S. Osella
Chemical and Biological Systems Simulation Lab, Centre of New Technologies
University of Warsaw,
Ochota campus, Banacha 2C, 02097 Warszawa, Poland

[c] M. Crisci, F. Schmitz, R. Altieri.
Institute of Physical Chemistry and Center for Materials Research (LaMa)
Justus Liebig University
Heinrich-Buff-Ring 17, 35392, Giessen, Germany

[d] Dr. H. Amenitsch, Dr. B. Sartori
Institute of Inorganic Chemistry,
Graz University of Technology,
Stremayrgasse 9, 8010, Graz, Austria

[e] Z. Liu
Nanochemistry Department,
Istituto Italiano di Tecnologia,
16163 Genova, Italy

[f] Dr. F. Lamberti
Dipartimento di Scienze Chimiche
Università degli Studi di Padova
Via Marzolo, 1, 35131, Padova, Italy
E-mail: francesco.lamberti@unipd.it

[g] Dr. F. Lamberti
Dipartimento di Ingegneria dell'Informazione
Università degli Studi di Padova
Via Gradenigo, 6b, 35131, Padova, Italy

[h] Dr. F. Lamberti
Zhejiang Beisheng Photovoltaic Co., Ltd.
No.800 Zhenbei Road, Zhili Town, Wuxing District Huzhou, Zhejiang 313000, China

Supporting information for this article is given via a link at the end of the document.

Abstract: The photoelectrocatalytic (PEC) hydrogen evolution reaction (HER) holds immense promise as a clean and sustainable method for hydrogen production. However, finding a suitable catalyst which is efficient, stable and scalable still remains an open challenge.

BiOBr is a 2D layered material studied as photoelectrocatalyst because of its suitable band gap for light absorption and potential for up-scalable production. However, its application in HER is not commonly reported, because of instability in a cathodic PEC environment, driven by a strong tendency to reduction to metallic bismuth. To solve this problem, 2D MoS_2 is used to induce the formation of a van der Waals (vdW) layered heterojunction (HJ) to stabilize the lattice of BiOBr during HER. By performing PEC HER with the HJs containing different ratios of MoS_2, it is found that the HJ with 1% MoS_2 can increase the stability of BiOBr, while the one with 50% MoS_2 can even accelerate the reduction of BiOBr to metallic bismuth. DFT calculations reveal that the interface between BiOBr and MoS_2 in the HJ with 1% MoS_2 tends to push active electrons on the sulfur atoms, thus favoring HER. On the other hand, in the 50% HJ, active electrons are prone to react with BiOBr to induce reduction. *In situ* wide-angle X-ray diffraction (WAXD) on the MoS_2/BiOBr HJs with 1% and 50% of MoS_2 allows to track the phase change and the phase transfer speed of BiOBr during PEC HER. Interestingly, when the HJ is illuminated with UV light, a lower amount of BiOBr is reduced to Bi under negative potential, due to the presence of photogenerated holes reacting with the extra electrons derived from the negative bias and preventing the BiOBr photon absorber to be further reduced.

Introduction

The photoelectrocatalytic hydrogen evolution reaction (PEC HER) is a fascinating and sustainable process, which harnesses sunlight and electric power to drive the production of hydrogen from water. However, several challenges such as efficiency, stability, cost and scalability still exist for optimizing photoelectrocatalysts for PEC HER.[1–3] BiOBr stands out as a promising photoelectrocatalyst with unique structural and electronic characteristics that make it well-suited for solar-driven applications.[4–6] Possessing a layered crystal structure with Bi_2O_2 layers separated by Br atoms, BiOBr has a peculiar electronic structure, which allows for efficient charge separation and migration, leading to enhanced PEC activity.[7] For instance, Ling et al. fabricated BiOBr nanosheet arrays on indium tin oxide as a photoanode and a transient current of 70 μA/cm^2 was detected at a bias of 0.9 V.[8] Wang et al. showed photocurrent density of 0.29 mA/cm^2 at 1.23 V vs. RHE for BiOBr.[9] Hu et al. used BiOBr nanosheets for PEC alcohol oxidation with the combination of Pt.[10] A BiOBr/Ti photoanode was used to degrade RhB under bias voltage of 0.7 V.[11] Meanwhile, its cost-effectiveness and potential for facile scaled-up production make BiOBr worthy to optimize as a photoelectrocatalyst.[12]

In most cases, however, the pure BiOBr is used as a photoanode suitable for oxidation reactions, due to its band structure.[13–15] *Operando* chemical stability is a critical factor in the practical application of BiOBr as a photoelectrocatalyst for HER. Since BiOBr has demonstrated reasonable stability only under specific conditions, research efforts are usually directed toward improving its resistance to photocorrosion, a process where the material degrades over prolonged exposure to light.[16] Meanwhile, the negative bias can cause the reduction of BiOBr as well, since the standard potential of Bi^{3+}/Bi^0 is 46 mV vs. Ag/AgCl.[17] In principle, the Bi- and BiO-terminations found in single-layer BiOBr demonstrate highly active sites for the HER, whereas the inert basal planes of monolayer BiOBr can be activated for the HER by introducing halogen vacancies.[18,19] Similarly, other BiOX compounds like BiOCl and BiOI may offer similar characteristics, but BiOBr remains the most extensively studied for the HER due to its optimal band-gap (2.42 eV).[20] Moreover, incorporating BiOBr with other materials could enhance its structural stability during PEC analysis. For instance, Shi et al. managed to reduce Cr(VI) to Cr(III) with MoS_2/BiOBr.[21] Han et al. fabricated core–shell structured Bi/BiOBr photoelectrode for PEC HER getting a photocurrent of 6 mA/cm^2 at -0.5 V vs. RHE.[22] A 2D MoS_2/BiOBr heterojunction (HJ) is a successful example to suppress self-reduction of the oxybromide during the PEC HER. In our previous work, it was found that within a few- layers MoS_2/BiOBr HJ, the BiOBr structure remains intact during the PEC HER only when the ratio of MoS_2 is 1%.[23] On the other hand, with 50% of MoS_2 inside the HJ, the BiOBr component is reduced to Bi in a short time.[23] However, the HJ with 1% of MoS_2 can only partially hinder the reduction process instead of completely avoiding it, and still a portion of BiOBr is reduced to Bi during PEC. Therefore, the methodology based on the selective modification of layered BiOBr for realizing HJs with cathodic properties is still at its infant stage and deeper mechanistic studies are required for its successful application in HER, at maximized stability.

Based on the above state-of-the-art situation, we present here a more detailed study on the PEC HER process with 2D MoS_2/BiOBr HJ catalysts. To dig more into the mechanism behind such system, we performed density functional theory (DFT) simulations to atomistically describe the HER process on the MoS_2/BiOBr HJ. Our calculations demonstrate that in the HJ with 50% MoS_2, active electrons are more likely to interact with BiOBr instead of reducing absorbed protons on sulfur atoms, leading to the production of metallic Bi. Conversely, in the 1%-MoS_2/BiOBr configuration, the interface between BiOBr and MoS_2 tends to transfer active electrons to the sulfur atoms, thereby promoting HER. Furthermore, we monitored the reduction process of BiOBr to metallic Bi in the HJs by synchrotron wide-angle X-ray diffraction (WAXD) during the PEC reaction. By comparing the HJs with 1% and 50% of MoS_2, the phase transfer in 50%-MoS_2/BiOBr results faster and more complete than that in 1%-MoS_2/BiOBr. More interestingly, under illumination conditions, there is less amount of BiOBr reduced compared to the same situation in dark. This happens most likely because photogenerated holes can neutralize the extra electrons and protect BiOBr from reduction to Bi.

Results and Discussion

The HJ samples are synthesized by a combination of microwave synthesis and liquid phase exfoliation (LPE) methods, as reported before and described briefly here in the experimental section.[20] By tuning the weight ratio of bulk BiOBr and MoS_2 precursors to 100:1 and 1:1, MoS_2/BiOBr van der Waals (vdW) HJs with few and large amount of MoS_2 are prepared. The sample with 1% of MoS_2 precursor is labelled as 1%-MoS_2/BiOBr, while the sample

with 50% of MoS_2 is labelled as 50%-MoS_2/BiOBr. The powder X-ray diffraction (P-XRD) patterns of 50%-MoS_2/BiOBr are indexed as the combination of a tetragonal BiOBr phase (ICSD number: 61225) and hexagonal MoS_2 phase (ICSD number: 95569) without the presence of any impurities (Figure S1). Only the BiOBr phase is instead detected in the 1%-MoS_2/BiOBr, because of the small content in MoS_2. Their morphologies were checked with transmission electron microscopy (TEM). As shown in Figure S2, pure exfoliated BiOBr and MoS_2 both provide nanosheets with irregular shape. 2D BiOBr shows a rough size range between 50 and 150 nm, while 2D MoS_2 is more than 300 nm in width. In Figure 1a and 1b, both 1%-MoS_2/BiOBr and 50%-MoS_2/BiOBr show the combination of large MoS_2 and small BiOBr nanosheets. The high-angle annular dark field scanning transmission electron microscopy (HAADF-STEM) and the corresponding STEM-EDX mapping of 1%-MoS_2/BiOBr displayed the existence of Mo and Bi elements, further confirming the existence of MoS_2 in 1%-MoS_2/BiOBr. The distribution of these two elements proved an overlapping of the two structures.

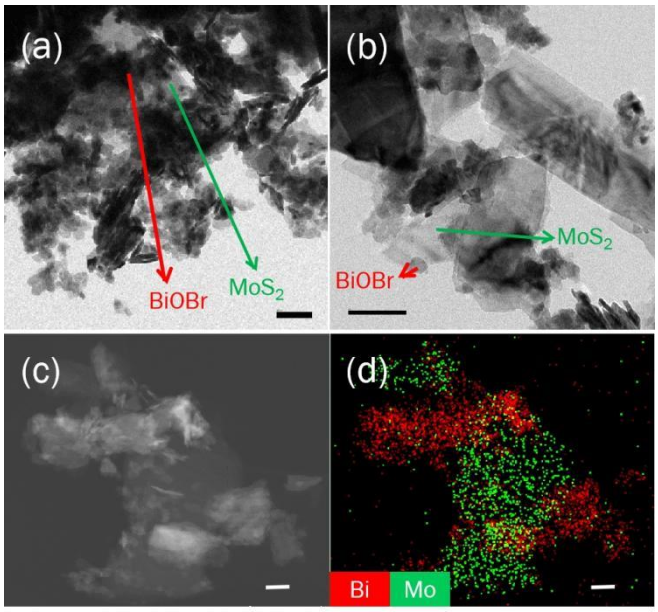

Figure 1. TEM images of (a) 1%-MoS_2/BiOBr and (b) 50%-MoS_2/BiOBr. (c) HAADF-STEM image and (d) EDX elemental mapping of 1%-MoS_2/BiOBr. Scale bars are 100 nm in all images.

Raman analysis was further performed to identify vdW interactions between BiOBr and MoS_2. Figure 2a depicts the Raman spectra for 2D layered BiOBr, 2D layered MoS_2, and 1%-MoS_2/BiOBr HJ excited by a 532 nm laser. The Raman spectrum of BiOBr presents a typical Raman peak of A_{1g} mode located at 125 cm^{-1} and a peak of E_{1g} mode located at 161 cm-1.[24] The A_{1g} and E_{1g} phonon modes come from the internal Bi-Br stretching vibration. These Raman peaks for pure BiOBr are consistent with those of the oxyhalide in the 1%-MoS_2/BiOBr HJ. On the other hand, in 50%-MoS_2/BiOBr, the characteristic peaks of BiOBr are weak and this is likely due to the large amount of MoS_2 covering the surface of the sample and fading signals from the pnictogen-containing species. The A_{1g} peak and E_{1g} peak of 1%-MoS_2/BiOBr demonstrate obvious red shift from 125 cm^{-1} and 161 cm^{-1} to 111

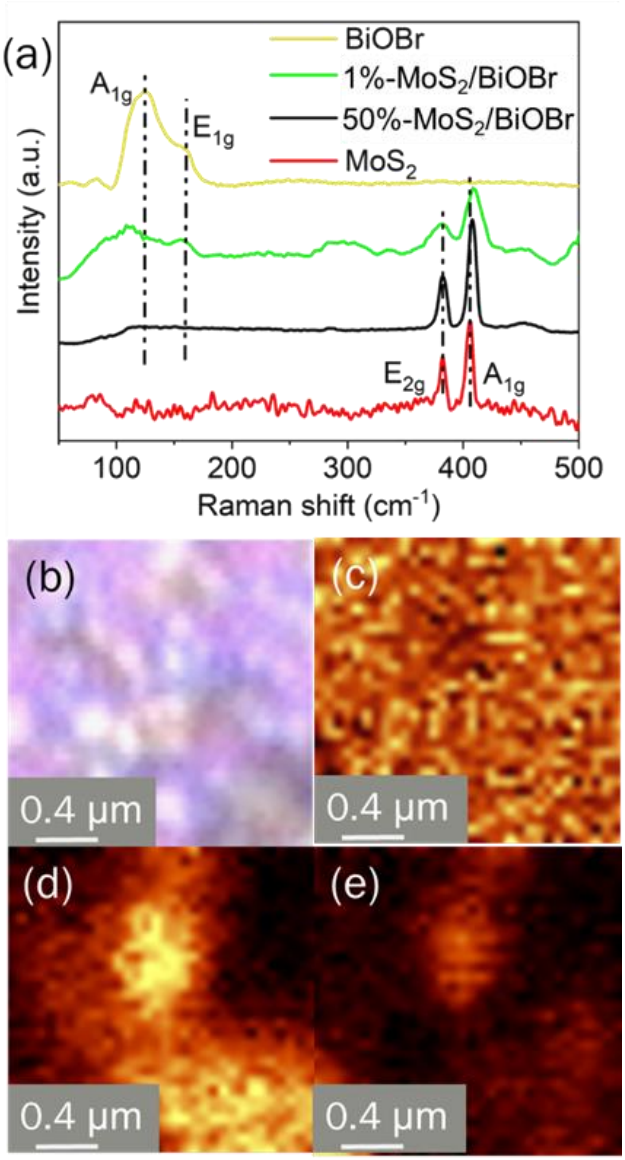

Figure 2. (a) Raman spectra of 2D BiOBr, 2D MoS_2 and 2D MoS_2/BiOBr HJs. At the selected area (b), Raman mapping of the peaks at (c) 125 cm^{-1}, (d) 409 cm^{-1}, and (e) 111 cm^{-1}.

cm^{-1} and 156 cm^{-1} compared with that of the pure BiOBr. The red shift reveals that the MoS_2/BiOBr vdW HJ is potentially associated with the interlayer coupling interaction of BiOBr and MoS_2 layers.[25–27] This might result from the Bi-S interaction, which has a lower frequency than Bi-Br.[28,29] The characteristic Raman peaks of MoS_2 are related to an in-plane phonon mode E_{2g} (382 cm^{-1}) of Mo-S and an out-of-plane phonon mode A_{1g} (406 cm^{-1}) of S-S bonds.[30] The difference between these two peaks are 24.3 cm^{-1}, which means the MoS_2 is exfoliated to few-layered materials, in a quasi 2D fashion.[31] As to the HJs, the position of E_{2g} is not changed apparently, while the position of A_{1g}, related to S-S bond, shows a blue shift to 409 and 408 cm^{-1} for 1%-MoS_2/BiOBr and 50%-MoS_2/BiOBr, respectively. This finding represents the initial evidence of surface sulfurs from MoS_2 forming an electrostatic van der Waals (vdW) interaction with BiOBr. Furthermore, the selected area in Figure 2b was analyzed through Raman mapping on a highly resolved nano-Raman set-

up.[32] It is clear form this further analysis that the BiOBr layered component is fully dispersed in this area. Figure 2c shows the integrated peak of BiOBr centered at 125 cm^{-1} with a peak width of 20 cm^{-1}, and Figure 2d displays the integrated peak from MoS_2 centered at 409 cm^{-1} with a peak width of 1 cm^{-1}, confirming the existence and distribution of BiOBr and MoS2 inside the area. Figure 2e shows the integration of the peak at 111 cm^{-1} (peak width of 5 cm^{-1}), which is from the HJ. Compared to Figure 2c, it is apparent that the peak at 111cm^{-1} only appears at the overlapping area of BiOBr and MoS_2 nanosheets, meaning that the interaction between the two components is among the whole overlapping area of BiOBr and MoS_2 nanosheets. Moreover, the deconvolution of the Mo 3d peaks in the X-ray photoelectron spectroscopy (XPS) spectra of the HJs revealed two peaks at 232.2 eV and 229.1 eV, corresponding to Mo^{4+} $3d_{3/2}$ and $3d_{5/2}$ in the 2H phase (Figure S3).[33] This demonstrates that only the 2H MoS_2 is present in the HJs and no traces of the metallic 1T-phase can be detected.

PEC HER has been conducted on photocathodes made of drop-casted MoS_2/BiOBr HJs and pure BiOBr on transparent conductive fluorine-doped tin oxide (FTO) substrates. As shown in Figure 3a and 3b, 50%-MoS_2/BiOBr and 1%-MoS_2/BiOBr yield -16.5 mA/cm^2 and -10 mA/cm^2 at -0.6 V vs. RHE in the first cycle, respectively. This significant enhancement in PEC activity, compared to pristine BiOBr (-3 mA/cm^2) in Figure 3c, suggests that the HJs exhibit more effective catalytic activity than pure BiOBr. However, the HER performance of 50%-MoS_2/BiOBr dropped dramatically from the second cycle, likely due to the reduction of BiOBr since the broad irreversible redox peak of $Bi^{3+}\rightarrow Bi^0$ appears before HER. Meanwhile, BiOBr has shown the redox peak of $Bi^{3+}\rightarrow Bi^0$ as well starting from the 2nd cycle, which is displayed in Figure 3c. Regarding 1%-MoS_2/BiOBr in Figure 3b, the redox peak appears from the 3rd cycle, and the current density for HER remains higher than -7 mA/cm^2 at -0.6 V vs. RHE after 5 cycles. In contrast, 50%-MoS_2/BiOBr shows almost no current after 3 cycles and BiOBr has sustain the low current density of ~-3 mA/cm^2. These results reveal that the HER activity and durability are highly related to the composition inside the HJ, which will be discussed in detail later.

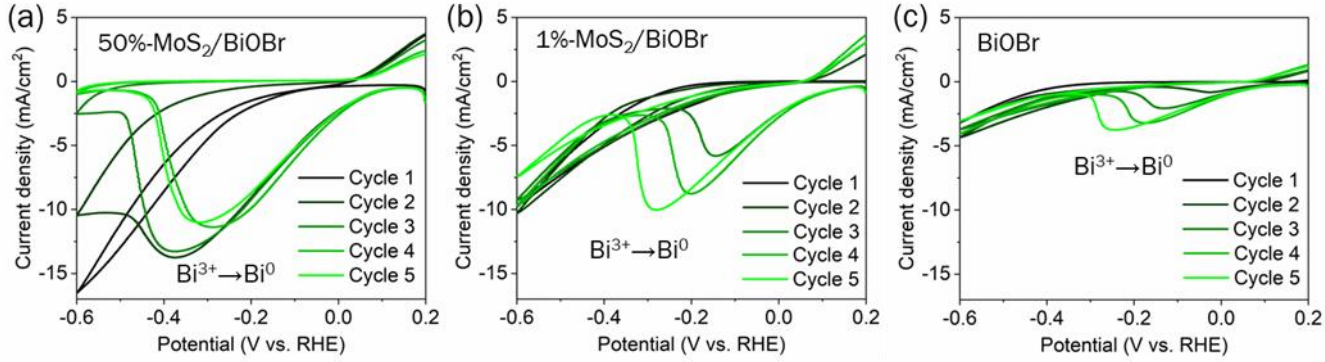

Figure 3. Cyclic voltammetries (CVs) of (a) 50%-MoS_2/BiOBr, (b) 1%-MoS_2/BiOBr and (c) pristine BiOBr.

DFT simulations were performed on the 50%-MoS_2/BiOBr to elucidate the HER mechanism, assuming the Mo-edge of MoS_2 as the reaction center. Since it has been reported in literature that the activity for HER linearly corelates with the amount of exposed edges in crystalline MoS_2, we consider here the same edges as active catalytic sites also at the interface.[34] As first step of the reaction, we consider the reduction of the interface while adding an electron ($[MoS_2]^-$), to mimic the experimental setup with applied potential at -0.5 V. The first hydrogen prefers to bind at the edge sulfur atom, rather than the molybdenum atom, resulting in strongly bonding interaction, with a calculated adsorption energy of -0.89 eV. Interestingly, no stable structures have been found for the Mo-H interaction. However, after considering solvent effects, entropy and vibrational corrections, the free energy for adding a hydrogen atom to the S edge is more stabilized, with value of -1.47 eV ($[MoS_2]H_S$). The first protonation occurs with the Volmer step, which is the potential-dependent step (PDS) of the reaction, with a maximum reaction free energy of 1.48 eV at -0.5 V vs standard hydrogen electrode (SHE). The PDS is the step leading to an intermediate which requires the highest energy to be obtained, being the limiting step of the whole reaction and possibly being the cause for a reaction pathway to be unfavorable; in the present case, this is correlated to a limiting potential U_L= -1.48 eV ($U_L=\Delta G_{PDS}/e$), meaning that to fully overcome this barrier, a potential of -1.5 V should be applied. The activation energy required to obtain the Volmer step is 1.73 eV at -0.5 V, making this first protonation also the rate determining step of the HER reaction. Adding a second proton to the Mo atom did not result in a stable structure, suggesting that the second H prefers to interact with a second S atom close to the first one. This second proton addition can occur either via Tafel or Heyrovsky mechanism. In the Tafel mechanism, a second proton is added to a S atom which neighbors the first one; in the Heyrovsky mechanism the second proton is added directly on top of the first proton (Figure 4a).[35–39] While both pathways are thermodynamically favorable, the Tafel one is the most active one, with a strong energy stabilization at -1.91 eV ($[MoS_2]H_SH_S$), while the Heyrovsky pathway only slightly stabilizes the system up to 1.24 eV ($[MoS_2]H_{S2}$). Interestingly, the Tafel step is virtually barrierless, while to obtain the Heyrovsky step a small activation barrier of 0.02 eV has to be overcome. Eventually, the hydrogen molecule is formed, with a Gibbs free energy stabilization of -2.14 eV ($[MoS_2]2H_S$, Figure 4a). As a

result, the $[MoS_2]$ → $[MoS_2]^-$ → $[MoS_2]H_S$ →$[MoS_2]H_SH_S$ →$[MoS_2]2H_S$ pathway can proceed with the first endergonic Volmer step, followed by a strongly exergonic Tafel step.

To assess the nature of the reduction pathways for the second proton transfer, we resort here to the analysis of the density of states and d-band center (Figure 4b and 4c). The strong thermodynamic stabilization of the Tafel intermediate is a result of upshift in the d-band center for the pristine surface compared to the Heyrovsky step. In fact, the d-band energy center has been found at -0.79 eV for the Heyrovsky step and is shifted up to -0.63 eV for the Tafel one. The main idea of this analysis is that the closer to the Fermi energy the metal d-band center is, the stronger the adsorbate-metal interaction is, due to a lower occupation of antibonding states. This is also confirmed by the density of states analysis, in which we observe that the antibonding states for the hydrogen atoms involved in the reaction are shifted up in energy, from 0.32 to 0.42 eV for the Heyrovsky and Tafel step, respectively. We believe that the high activation energy barrier observed from the 50%-MoS_2/BiOBr explains the observed experimental behavior; at such elevated concentration of BiOBr, it might be easier for the Bi to become metallic than for the reaction to proceed, in all the potential range observed. Hence, after a few cycles the HER production comes to a stop. On the other hand, when the percentage of MoS_2 is decreased to 1% at the interface, the smaller presence of Bi allows for the HER to continue for more cycles. Changing the potential to more negative values lead to overall stabilization of the Volmer intermediate and the related transition state. However, while the energy of the $[MoS_2]H_S$ intermediate strongly decreases, going from 1.73 eV at U=-0.25 V to 0.48 eV at U= -1.5 V, the decrease in the energy barrier for this step is rather small, from 1.86 at U=-0.25 V to 1.23 eV at U=-1.5 V (Figure 4d). The lower energy predicted at -1.6 V confirms that this key intermediate can be strongly stabilized, ensuring the PEC of the interface even for the 50%-MoS_2/BiOBr for more cycles. Now, it becomes crucial to consider the stability of the entire interface. As the applied potential becomes more negative, the interface may become more susceptible to deterioration, possibly resulting in additional reduction of Bi to its metallic form.

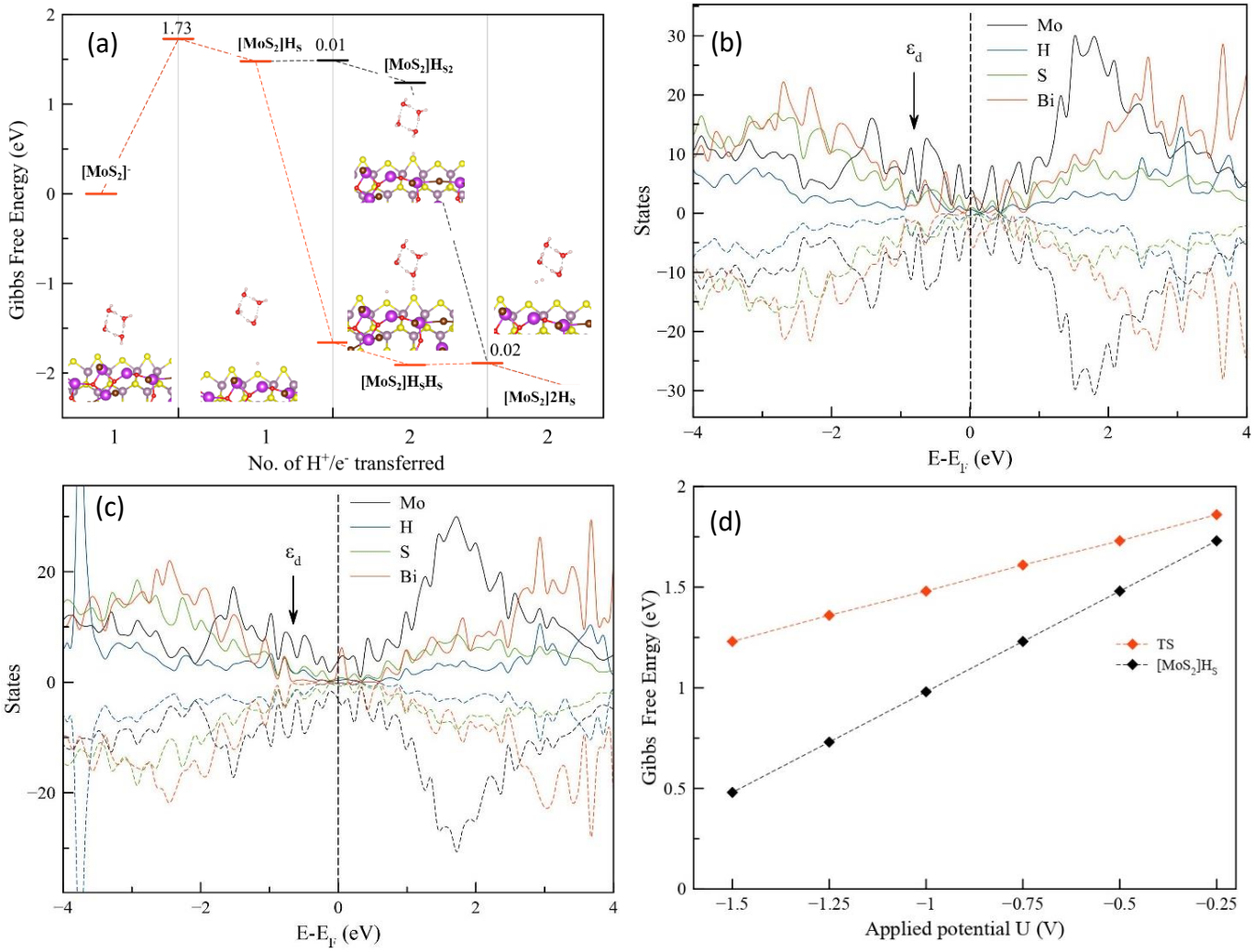

Figure 4. (a) Gibbs free energy reaction pathway for the HER formation at the MoS_2/BiOBr interface, at an applied potential of -0.5 V. Transition states are also reported, as well as the activation energy. Density of states (DOS) on the 3d orbitals for Mo and Bi metal centres, 2p orbitals of S and s orbitals for H for (b) Heyrovsky and (c) Tafel step. (d) Relative Gibbs free energy of the Volmer step and the associated transition state at various applied potentials.

To comprehensively understand the impact of the composition of the HJs on the PEC HER activity, *in-situ* WAXD was conducted during the PEC HER. Figure 5a-c record a clear phase change of BiOBr from *in-situ* XRD diffractograms of 1%-MoS_2/BiOBr, 50%-MoS_2/BiOBr and pristine BiOBr after each cycle of HER and the patterns with selected ranges of 18.5-25 nm^{-1} of q vectors. Before the catalytic reaction, all the samples display two broad diffraction peaks centered at 22.9 and 23.3 nm^{-1}, which are attributed to the BiOBr phase. Further performing the CVs under PEC environment made gradual formation of Bi from BiOBr, as the intensity of the characteristic peak of metallic Bi at 19.7 nm^{-1} increased continuously, while the intensity of the peaks belonging to BiOBr decreased. When comparing these three samples, it is evident that the phase change inside 50%-MoS_2/BiOBr is much faster than that in 1%-MoS_2/BiOBr and BiOBr. The reduction of BiOBr in 50%-MoS_2/BiOBr and pristine BiOBr is complete after 1 cycle and 3 cycles of PEC reaction, respectively, while 1%-MoS_2/BiOBr can reserve the original BiOBr phase after 5 cycles of reactions. Moreover, the peak intensity ratio of the peaks at 22.9 and 19.7 nm^{-1} is calculated in Figure 6 to compare the phase change of the samples. For 50%-MoS_2/BiOBr, the peak ratio is close to 0 after the first cycle, while the value of 1%-MoS_2/BiOBr remains more than 0.5 after 5 cycles. Given that the peak ratio of pristine BiOBr diminishes to 0 after 3 cycles, it becomes evident that the HJ with just 1% of MoS_2 plays a crucial role in mitigating the reduction of the BiOBr component.

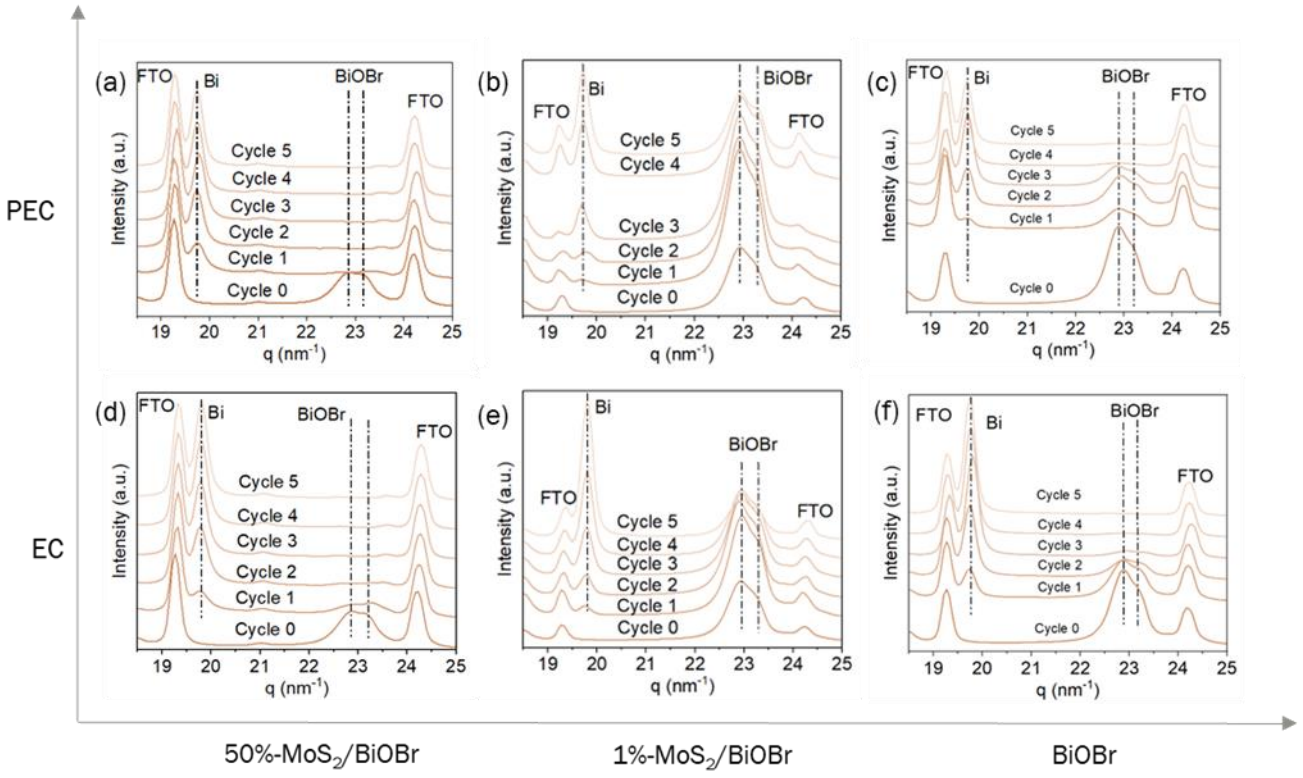

Figure 5. *In situ* WAXD of (a) 50%-MoS_2/BiOBr, (b) 1%-MoS_2/BiOBr and (c) pristine BiOBr during PEC HER, and (d) 50%-MoS_2/BiOBr, (e) 1%-MoS_2/BiOBr and (f) pristine BiOBr during EC HER.

To correlate these findings with the CVs presented in Figure 3, it can be inferred that MoS_2/BiOBr serves as an efficient photoelectrocatalyst, whereas MoS_2/Bi exhibits minimal activity in PEC HER. Therefore, it is important to maintain BiOBr from reducing to Bi. According to the previous DFT calculations, in such a type-I HJ, the small amount of MoS_2 (in 1%-MoS_2/BiOBr) not only attracts photogenerated electrons and provides active sites for HER, but also contains a suitable valence band position which can prevent the transfer of photogenerated holes from BiOBr.[23] In this case, the remaining photogenerated holes on BiOBr can neutralize part of the electrons from UV light or negative bias and protect BiOBr from being reduced. However,

these photogenerated holes are not enough to neutralize all the extra electrons inside BiOBr, thus there is a part of BiOBr reduced to Bi after each CV. Conversely, an increasing ratio of MoS_2 inside the HJ changes the band structure and photogenerated holes start to migrate to MoS_2. Without the photogenerated holes staying on BiOBr, BiOBr is rapidly reduced to Bi by electrons from electric field or photo energy.[23] When considering influence of the outside electric field, the DFT calculations demonstrate that before the HER happens, the negative potential can destroy the stability of the interface inside the 50%-MoS_2/BiOBr and form a large amount of Bi on the interface firstly (Figure 4). This combination of MoS_2 and Bi is not favorable for HER, unfortunately.

In order to prove the function of the photogenerated holes in stabilizing the structure of BiOBr, we measured the phase change of the samples under purely electrocatalytic (EC) conditions (in dark). As compared in Figure 5b and 5e, within the 1%-MoS_2/BiOBr HJ, it is surprising to observe that the formation of Bi is always less under PEC condition than under EC condition, as the BiOBr/Bi peak ratio under illumination is much higher than in dark after each cycle (Figure 6). A similar trend is found for pristine BiOBr as well (Figure 5c, 5f and 6). On the other side, for 50%-MoS_2/BiOBr, there is no apparent difference since BiOBr is reduced rapidly both under PEC and EC conditions (Figure 5a and 5d), and the peak intensity ratio of BiOBr/Bi is below 1 after the 1st cycle (Figure 6). The phase change of 1%-MoS_2/BiOBr and BiOBr reveals that the UV light does not accelerate the reduction of BiOBr under PEC condition, because the photogenerated holes protect BiOBr from reduction in the PEC environment, while the photogenerated electrons are transferred on the surface of MoS_2 for HER or charge recombination.

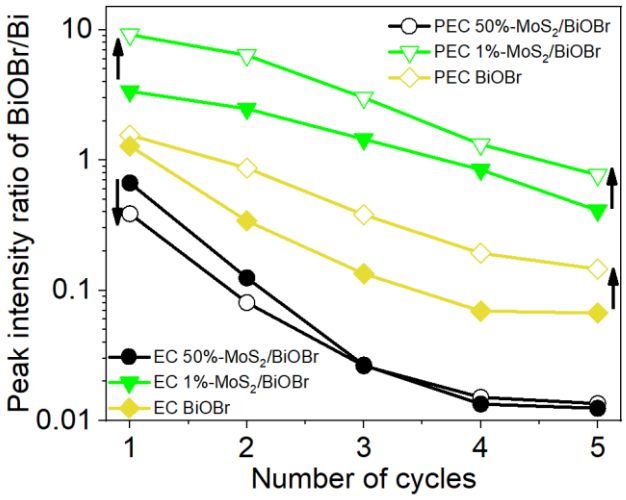

Figure 6. Peak intensity ratios of the peaks at 22.9 (belonging to BiOBr) and 19.7 nm^{-1} (belong to Bi).

Conclusion

In this work, we show the PEC HER performance of layered MoS_2/BiOBr vdW HJs containing different ratios of the two components and analyze their catalytic mechanism, through a joint experimental-theoretical approach. From the measurement of PEC HER activity, emerges a counterintuitive better durability behaviour of the 1%-MoS_2/BiOBr HJ with respect to the 50%-MoS_2/BiOBr. DFT calculations point out, in fact, that the vdW interface in 50%-MoS_2/BiOBr is easier to collapse, and electrons prefer to react with BiOBr instead of the absorbed protons on the edged S sites. In addition, *in situ* WAXD shows a phase change of BiOBr to Bi during the HER. By comparing phase change between 1%-MoS_2/BiOBr and 50%-MoS_2/BiOBr, it is clear that BiOBr is reduced to Bi more rapidly in 50%-MoS_2/BiOBr than in 1%-MoS_2/BiOBr. On one side, in 1%-MoS_2/BiOBr the band structure is more suitable for distributing active electrons for HER; on the other side, under bias, BiOBr in the 50%-MoS_2/BiOBr reduces fastly to Bi and hinders the HER. More importantly, by comparing the phase change under EC and PEC conditions, it is proved that under UV light, the reduction of BiOBr slows down because the photogenerated holes can partially protect the BiOBr phase. The insights here presented on the PEC HER mechanism in this specific layered HJs may be applicable to other analogous systems and thereby enable the future design and development of novel nano-sized heterogeneous catalysts with high efficiency and stability.

Experimental details

Materials

Bismuth(III) nitrate pentahydrate ($Bi(NO_3)_3{\cdot}5H_2O$), potassium bromide (KBr), ethylene glycol (EG), molybdenum(IV) sulfide (MoS_2), N-methyl-2-pyrrolidone (NMP), ethanol and FTO glass substrates were purchased from Sigma-Aldrich. Milli-Q water was sourced using the Milli-Q ultrapure system for all experiments.

Preparation of photoelectrocatalysts

To synthesize BiOBr microspheres, a solvothermal method, adapted from Shi et al. was employed using $Bi(NO_3)_3{\cdot}5H_2O$ and KBr as precursors.[40] Initially, 83.3 mg of KBr were dissolved in 10 mL of EG, followed by the addition of 339.5 mg of $Bi(NO_3)_3{\cdot}5H_2O$ to the solution. The mixture was stirred for 30 minutes at room temperature, then transferred to a 40 mL Teflon autoclave for solvothermal treatment at 120 °C for 12 hours. After cooling naturally, the white sample was collected, washed with ethanol and H_2O to remove any unreacted chemicals and impurities.

To create HJs, multilayer MoS_2 was first obtained through liquid phase exfoliation (LPE) using a tip-sonicator for 9 hours with 500 mL of H_2O and 5 g of MoS_2 powder. The resulting mixture was centrifuged at 2000 rpm for 20 minutes, and the suspension was collected. Afterward, the suspension was centrifuged at 8000 rpm for 5 minutes to precipitate the multilayer MoS_2, which served as a precursor for the subsequent steps. Next, the BiOBr microspheres and multilayer MoS_2 were added to 50 mL of NMP for further LPE, with 9 hours of tip-sonication to achieve heterojunction formation. For the 1%-MoS_2/BiOBr configuration, 2

mg of MoS_2 and 200 mg of BiOBr were added, while for the 50%-MoS_2/BiOBr setup, 100 mg of MoS_2 and 100 mg of BiOBr were added. After centrifuging the mixture at 2000 rpm for 20 minutes, stable colloidal suspensions were obtained. Finally, ethanol and water were added to precipitate the products.

Characterization

Brightfield TEM (BF-TEM) imaging was conducted using a JEOL JEM-1011 instrument with an acceleration voltage of 100 kV. To prepare the samples, dilute suspensions of the nanomaterials in ethanol were dropped onto carbon film-coated 200 mesh copper grids. For HRTEM HAADF-STEM imaging and STEM-EDX analyses, an image-Cs-corrected JEOL JEM-2200FS TEM equipped with a Bruker X-Flash 5060 SDD was operated at 200 kV. Holey-amorphous carbon films on Cu grids served as support for these analyses. We characterized samples using a WITec confocal Raman system (α300-Raman WITec GmbH, Ulm, Germany), equipped with a 100X Zeiss objective, NA = 0.9 and a dispersive grating of 600 gr/mm that images a 100 µm core fiber, used to couple microscope to the f = 320 mm spectrometer, as the input slit aperture on a 1 × 2048 pixels CCD (Newtown CCD, Andor, −80°C thermoelectric cooled). A solid-state laser, 532 nm, power of 14 mW, was used as the excitation line. The samples were dropped on n-type Si wafer. For the Raman spectra, each measure was obtained accumulating 80 spectra, each with an integration time of 25 s. Raman spectroscopy maps of 4 × 4 µm and 48 × 48 points were acquired at 2 seconds integration time per point. XPS spectra were acquired using a spectrometer manufactured by Physical Electronics GmbH (PHI 5000 VersaProbe II).

(Photo)electrochemical measurements

EC and PEC HER tests were conducted using a three-electrode photoelectrochemical reaction cell immersed in a 0.5 M Na_2SO_4 electrolyte solution. The reference electrode utilized was Ag/AgCl (saturated KCl electrolyte), while the counter electrode consisted of a platinum wire. For the PEC HER experiments, the samples were air-dried and subsequently dispersed in ethanol at a concentration of 5 mg mL^{-1}. Ink solutions of 0.12 mL were drop-cast onto conductive FTO glass substrates. A mercury lamp with a light intensity of 16 mW cm^{-2} served as the light source. Potentiostatic tests were carried out using an Autolab instrument, while CVs were performed at a scan rate of 50 mV s^{-1} within the range of 0.2 to −0.6 V vs. RHE.

In situ WAXD characterizations

In situ wide WAXD measurements were performed at the Austrian SAXS beamline of the Elettra Sincrotrone in Trieste.[41] The beamline has been adjusted to a q-resolution ($q = 4\pi/\lambda * \sin(2\theta/2)$) between 18 and 47 nm^{-1} using an X-ray energy of 8 keV. For each sample, the WAXD data was collected after each CV.

Computational details

Details on the construction of the interface have been reported in our previous study. Briefly, all calculations were performed using spin-polarized density functional theory (DFT) as implemented in the Vienna ab initio simulation package (VASP).[42–44] The Perdew-Burke-Emzerhof (PBE) functional with a plane-wave cutoff energy of 500 eV was used. The structural optimizations were centered at Gamma. A vacuum space of 3 nm in the *y* direction (along interface edges) and of 1.5 nm along the *z* direction (perpendicular to the basal plane) were used to avoid interactions between periodic images. The convergence criteria for the force on each atom was set to 0.02 eV/Å, while the electronic structure energy convergence criteria was 10^{-5} eV. The Grimme D3 method with Becke-Johnson parameters[45] were employed to account for Van der Waals interactions.[46] The vibrational modes were calculated at 298.15 K to obtain the zero-point energy, entropy, and temperature corrections to enthalpy.

To accurately describe proton transfer from water solvent to the reactant, we considered the solvent as follows: a four-water molecule cage was added to the system close to the reaction center, to enable the proton transfer process. Moreover, the whole system was also surrounded by implicit water solvent, giving an additional layer of solvation which can affect the catalysis. The implicit solvent was considered within the VASPsol method.

The coupled proton-electron transfer (CPET) reactions were modelled using the computational hydrogen electrode (CHE) of Norskov.[47] In this approach, the voltage of reference (zero) is defined as for the reversible hydrogen electrode (RHE), where gas-phase hydrogen is converted into protons and electrons (reversibly) at zero volts ($H^+ + e^- \rightarrow ½\ H_2$). Because this reaction is in equilibrium, one can make the approximation that the chemical potential of the proton-electron pair, $\mu(H^+) + \mu(e^-)$, equals half of the chemical potential of gas-phase H_2, $1/2\mu(H_2)$. As a result, the chemical potential of the proton-electron pair can be adjusted based on the applied potential (U) with the equation (1):

$$\mu(H^+) + \mu(e^-) \rightarrow 1/2\mu(H_2) - eU \qquad (1)$$

where *e* is the elementary positive charge. It is assumed that both proton and electron transfer occur in concert during an electrochemical step. For all of the electrochemical steps along the reaction path, the free energy change between intermediates was computed to indicate the feasibility of the electrochemical process, *i.e.*, no energy barriers were calculated. Based on the computational hydrogen electrode (CHE) model, the Gibbs free energy change (ΔG) was calculated using Equation (2):

$$\Delta G = \Delta E_{DFT} + \Delta E_{ZPE} - T\Delta S + kTln10\ x\ pH - eU \qquad (2)$$

where ΔE_{DFT} is the total energy from DFT simulations, ΔE_{ZPE} is the zero-point energy calculated from vibrational frequencies, T is the temperature (298.15 K), S is the entropy obtained from vibrational frequencies, k is the Boltzmann constant, pH = 7 and U is the electrode potential (-0.5 V). Zero point energy and entropic contribution were directly obtained from frequency calculations using VASPKIT.[48] Activation energies were computed using the Brønsted–Evans–Polanyi (BEP) relationship,[30,31] which relates the kinetic barrier to the corresponding reaction energy for a class of materials.

The d band center (ε_d) for the metal atom involved in the catalysis around the adsorption sites is given by

$$\varepsilon_d = \frac{\int_{-\infty}^{+\infty} \rho(E)(E-E_F)\,dE}{\int_{-\infty}^{+\infty} (E-E_F)\,dE} \qquad (3)$$

where ρ(E) is the density of state (DOS) projected on the d-states of the metal atoms and E_F is the Fermi energy of the system.

Acknowledgements

M.W. and T.G. thank Fondazione Compagnia di San Paolo for financial support through the "Bando TRAPEZIO - Paving the way to research excellence and talent attraction" and through the program "Attrazione e retention di docenti di qualità". T.G. would like to acknowledge the support of the European Research Council for the project JANUS BI (grant agreement no. [101041229]). M.C. and T.G. thank the European Commission for the project LIGHT CAP (grant agreement no. [101017821]). R.A. thanks the DFG for project no. 460609161. S.O. thanks the National Science Centre, Poland (grant no. UMO/2020/39/I/ST4/01446) and the "Excellence Initiative – Research University" (IDUB) Program, Action I.3.3 – "Establishment of the Institute for Advanced Studies (IAS)" for funding (grant no. UW/IDUB/2020/25). The computation was carried out with the support of the Interdisciplinary Center for Mathematical and Computational Modeling at the University of Warsaw (ICM UW) under grants no. G83-28 and GB80-24. We acknowledge Elettra - Sincrotrone Trieste for provision of synchrotron radiation facilities (proposal no. 20222129). Sigrid Bernstorff is acknowledged for help during the WAXD measurements.

Keywords: Photoelectrochemistry, hydrogen evolution reaction, van der Walls heterojuction, transition metal dichalcogenide, bismuth oxyhalide

References

[1] S. Kumaravel, E. Kim, B. B. Kale, A. Adhikari, R. Patel, S. Kundu, *ChemElectroChem* **2022**, *9*, e202200724.

[2] E. Kemppainen, A. Bodin, B. Sebok, T. Pedersen, B. Seger, B. Mei, D. Bae, P. C. K. Vesborg, J. Halme, O. Hansen, P. D. Lund, I. Chorkendorff, *Energy Environ. Sci.* **2015**, *8*, 2991.

[3] C. Ding, J. Shi, Z. Wang, C. Li, *ACS Catal.* **2017**, *7*, 675.

[4] S. Lin, Y. Chen, J. Fu, L. Sun, Q. Jiang, J. F. Li, J. Cheng, C. Lin, Z. Q. Tian, *Int. J. Hydrogen Energy* **2022**, *47*, 41553.

[5] S. S. Imam, R. Adnan, N. H. Mohd Kaus, *J. Environ. Chem. Eng.* **2021**, *9*, 105404.

[6] W. Li, X. Wang, Y. Zhang, S. Zhu, M. Zhao, H. Zhang, Y. Wang, D. Zhang, W. Ran, L. Zhang, N. Li, T. Yan, W. Li, X. Wang, Y. Zhang, S. Zhu, M. Zhao, H. Zhang, Y. Wang, D. Zhang, W. Ran, L. Zhang, N. Li, T. Yan, *Adv. Mater. Interfaces* **2022**, *9*, 2200260.

[7] B. Q. L. Low, W. Jiang, J. Yang, M. Zhang, X. Wu, H. Zhu, H. Zhu, J. Z. X. Heng, K. Y. Tang, W. Y. Wu, X. Cao, X. Q. Koh, C. H. T. Chai, C. Y. Chan, Q. Zhu, M. Bosman, Y. W. Zhang, M. Zhao, Z. Li, X. J. Loh, Y. Xiong, E. Ye, *Small Methods* **2023**, 2301368.

[8] Y. Ling, Y. Dai, J. Zhou, *J. Colloid Interface Sci.* **2020**, *578*, 326.

[9] Z. Q. Wang, H. Wang, X. F. Wu, T. L. Chang, *J. Alloys Compd.* **2020**, *834*, 155025.

[10] J. Hu, C. Zhai, C. Yu, L. Zeng, Z. Q. Liu, M. Zhu, *J. Colloid Interface Sci.* **2018**, *524*, 195.

[11] K. Li, H. Zhang, Y. Tang, D. Ying, Y. Xu, Y. Wang, J. Jia, *Appl. Catal. B Environ.* **2015**, *164*, 82.

[12] K. Dai, D. Li, J. Lv, L. Lu, C. Liang, G. Zhu, *Mater. Lett.* **2014**, *136*, 438.

[13] L. W. Duresa, D. H. Kuo, F. T. Bekena, W. L. Kebede, *J. Phys. Chem. Solids* **2021**, *156*, 110132.

[14] S. S. Liu, Q. J. Xing, Y. Chen, M. Zhu, X. H. Jiang, S. H. Wu, W. Dai, J. P. Zou, *ACS Sustain. Chem. Eng.* **2019**, *7*, 1250.

[15] S. Vinoth, A. Pandikumar, *Renew. Energy* **2021**, *173*, 507.

[16] X. Tu, X. Zhou, S. Ke, Z. Zeng, *Mater. Technol.* **2022**, *37*, 1298.

[17] M. Malys, G. Fafilek, C. Pirovano, R. N. Vannier, *Solid State Ionics* **2005**, *176*, 1769.

[18] H. X. Pan, L. P. Feng, W. Zeng, Q. C. Zhang, X. D. Zhang, Z. T. Liu, *Inorg. Chem.* **2019**, *58*, 13195.

[19] H. Pan, L. Feng, S. Liu, Z. Li, H. Guo, P. Liu, X. Zheng, X. Zhang, J. Liu, *Int. J. Hydrogen Energy* **2022**, *47*, 1683.

[20] X. Wang, Z. Chen, J. Zheng, Y. Li, X. Peng, X. Zhang, H. Yin, X. Xiong, J. Duan, X. Li, Z. Wang, Z. Chen, J. Han, W. Xiao, Y. Yao, *ACS Appl. Energy Mater.* **2020**, *3*, 11848.

[21] Z. Shi, Y. Zhang, G. Duoerkun, W. Cao, T. Liu, L. Zhang, J. Liu, M. Li, Z. Chen, *Environ. Sci. Nano* **2020**, *7*, 2708.

[22] J. Han, Y. Gao, Y. Li, Z. Chen, X. Liu, X. Xiong, X. Zhang, Y. Jiang, Q. Luo, Y. Song, Z. Wang, X. Li, Z. Chen, W. Xiao, *J. Phys. Chem. C* **2020**, *124*, 24164.

[23] M. Wang, S. Osella, R. Brescia, Z. Liu, J. Gallego, M.Cattelan, M. Crisci, S. Agnoli, T. Gatti, *Nanoscale* **2023**, *15*, 522.

[24] M. M. Ferrer, J. E. F. S. Rodrigues, M. A. P. Almeida, F. Moura, E. Longo, P. S. Pizani, J. R. Sambrano, *J. Raman Spectrosc.* **2018**, *49*, 1356.

[25] J. H. Yu, H. R. Lee, S. S. Hong, D. Kong, H. W. Lee, H. Wang, F. Xiong, S. Wang, Y. Cui, *Nano Lett.* **2015**, *15*, 1031.

[26] F. Neubrech, D. Weber, J. Katzmann, C. Huck, A. Toma, E. Di Fabrizio, A. Pucci, T. Härtling, *ACS Nano* **2012**, *6*, 7326.
[27] M. Cottat, C. D'andrea, R. Yasukuni, N. Malashikhina, R. Grinyte, N. Lidgi-Guigui, B. Fazio, A. Sutton, O. Oudar, N. Charnaux, V. Pavlov, A. Toma, E. Di Fabrizio, P. G. Gucciardi, M. Lamy De La Chapelle, *J. Phys. Chem. C* **2015**, *119*, 15532.
[28] S. R. Zhu, Q. Qi, W. N. Zhao, Y. Fang, L. Han, *J. Phys. Chem. Solids* **2018**, *121*, 163.
[29] X. Guo, Y. T. Huang, H. Lohan, J. Ye, Y. Lin, J. Lim, N. Gauriot, S. J. Zelewski, D. Darvill, H. Zhu, A. Rao, I. McCulloch, R. L. Z. Hoye, *J. Mater. Chem. A* **2023**, *11*, 22775.
[30] M. Thripuranthaka, R. V. Kashid, C. Sekhar Rout, D. J. Late, *Appl. Phys. Lett.* **2014**, *104*, 081911.
[31] H. Li, Q. Zhang, C. C. R. Yap, B. K. Tay, T. H. T. Edwin, A. Olivier, D. Baillargeat, *Adv. Funct. Mater.* **2012**, *22*, 1385.
[32] A. Giugni, B. Torre, M. Allione, G. Das, Z. Wang, X. He, H. N. Alshareef, E. Di Fabrizio, A. Giugni, B. Torre, M. Allione, G. Das, E. Di Fabrizio, Z. Wang, X. He, H. N. Alshareef, *Adv. Opt. Mater.* **2017**, *5*, 1700195.
[33] W. Wei, K. Sun, Y. H. Hu, *J. Mater. Chem. A* **2016**, *4*, 12398.
[34] T. F. Jaramillo, K. P. Jørgensen, J. Bonde, J. H. Nielsen, S. Horch, I. Chorkendorff, *Science (80-.).* **2007**, *317*, 100.
[35] J. Durst, A. Siebel, C. Simon, F. Hasché, J. Herranz, H. A. Gasteiger, *Energy Environ. Sci.* **2014**, *7*, 2255.
[36] D. Strmcnik, P. P. Lopes, B. Genorio, V. R. Stamenkovic, N. M. Markovic, *Nano Energy* **2016**, *29*, 29.
[37] X. Tian, P. Zhao, W. Sheng, X. Tian, P. Zhao, W. Sheng, *Adv. Mater.* **2019**, *31*, 1808066.
[38] Y. Zheng, Y. Jiao, M. Jaroniec, S. Z. Qiao, *Angew. Chemie Int. Ed.* **2015**, *54*, 52.
[39] N. Krstajić, M. Popović, B. Grgur, M. Vojnović, D. Šepa, *J. Electroanal. Chem.* **2001**, *512*, 16.
[40] X. Shi, X. Chen, X. Chen, S. Zhou, S. Lou, Y. Wang, L. Yuan, *Chem. Eng. J.* **2013**, *222*, 120.
[41] H. Amenitsch, M. Rappolt, M. Kriechbaum, H. Mio, P. Laggner, S. Bernstorff, *urn:issn:0909-0495* **1998**, *5*, 506.
[42] G. Kresse, J. Furthmüller, *Phys. Rev. B* **1996**, *54*, 11169.
[43] G. Kresse, J. Hafner, *Phys. Rev. B* **1994**, *49*, 14251.
[44] G. Kresse, J. Furthmüller, *Comput. Mater. Sci.* **1996**, *6*, 15.
[45] S. Grimme, S. Ehrlich, L. Goerigk, *J. Comput. Chem.* **2011**, *32*, 1456.
[46] S. Grimme, J. Antony, S. Ehrlich, H. Krieg, *J. Chem. Phys.* **2010**, *132*.
[47] J. K. Nørskov, J. Rossmeisl, A. Logadottir, L. Lindqvist, J. R. Kitchin, T. Bligaard, H. Jónsson, *J. Phys. Chem. B* **2004**, *108*, 17886.
[48] V. Wang, N. Xu, J. C. Liu, G. Tang, W. T. Geng, *Comput. Phys. Commun.* **2021**, *267*, 108033.

Entry for the Table of Contents

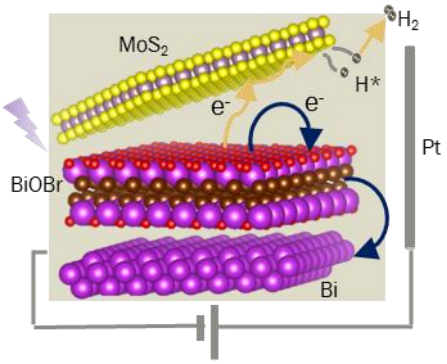

In MoS_2/BiOBr photocathode, the active electrons from both UV light and electric field can either reduce the adsorbed H* on the edge of MoS_2 to H_2 or reduce BiOBr to Bi. Varying the MoS_2 content in the HJ impacts the stability of BiOBr in PEC HER. HJs with 1% MoS_2 enhance BiOBr stability, while those with 50% accelerate BiOBr reduction.